

## Giant injection-locking bandwidth of a self-pulsing limit-cycle in an optomechanical cavity

Daniel Navarro-Urrios <sup>1✉</sup>, Guillermo Arregui<sup>2</sup>, Martín F. Colombano<sup>1,3</sup>, Juliana Jaramillo-Fernández <sup>1</sup>, Alessandro Pitanti <sup>4</sup>, Amadeu Griol<sup>5</sup>, Laura Mercadé <sup>1,5</sup>, Alejandro Martínez <sup>5</sup> & Néstor E. Capuj<sup>6,7</sup>

Locking of oscillators to ultra-stable external sources is of paramount importance for improving close-to-carrier phase noise in free running oscillators. In most of them, such as Micro-Electro-Mechanical-Systems or LC circuit-based oscillators, the locking frequency range is limited by the robustness of their natural frequency, which comes explicitly related with intrinsic parameters of the system. In this work we report the synchronization of an optically-driven self-pulsing limit-cycle taking place in a silicon optomechanical crystal cavity to an external harmonic signal that modulates the driving laser. Because of the extreme ductility of the natural self-pulsing frequency (several tens of MHz), the injection-locking mechanism is highly efficient and displays giant relative bandwidths exceeding 60%. The external modulation reveals itself as a knob to explore dynamical attractors that are otherwise elusive and, in particular, as a means to initialize a mechanical resonator into a state of self-sustained oscillations driven by radiation pressure forces. Moreover, we exploit the large anharmonicity of the studied limit-cycle to induce injection-locking to integer multiples and fractions of the frequency of the external reference, which can be used for frequency conversion purposes in nano-electro-opto-mechanical systems.

<sup>1</sup> MIND-IN2UB, Departament d'Enginyeria Electrònica i Biomèdica, Facultat de Física, Universitat de Barcelona, Martí i Franquès 1, 08028 Barcelona, Spain. <sup>2</sup> Department of Photonics Engineering, DTU Fotonik, Technical University of Denmark, Building 343, DK-2800 Kgs Lyngby, Denmark. <sup>3</sup> Université Paris Cité, CNRS, Laboratoire Matériaux et Phénomènes Quantiques, 75013 Paris, France. <sup>4</sup> NEST, Istituto Nanoscienze—CNR and Scuola Normale Superiore, Piazza San Silvestro 12, I-56127 Pisa, Italy. <sup>5</sup> Nanophotonics Technology Center, Universitat Politècnica de València, València 46022, Spain. <sup>6</sup> Depto. Física, Universidad de La Laguna, 38200 San Cristóbal de La Laguna, Spain. <sup>7</sup> Instituto Universitario de Materiales y Nanotecnología, Universidad de La Laguna, 38071 Santa Cruz de Tenerife, Spain. ✉email: [dnavarro@ub.edu](mailto:dnavarro@ub.edu)

It is a well-known phenomenon that a self-sustained oscillator can be synchronized to a weak external signal if the frequency of the latter is near the natural frequency of the former<sup>1,2</sup>. There are many diverse examples of such unidirectional mechanism in our everyday life, such as the circadian rhythms of cells originating from the rotation of the Earth around its axis and around the Sun, the entrainment of the breathing of anesthetized human with mechanical ventilators or the working principle of a radio-controlled watch. The dynamics of injection-locked oscillators have been explored extensively since the pioneer study of Adler<sup>3</sup> and others afterwards<sup>4–7</sup> and many applications came since then. In the last decades, injection locking methods have been increasingly exploited in oscillators of various natures for applications in the distribution of clock signals<sup>8,9</sup> as well as in frequency synthesis<sup>10,11</sup>, among others.

Here we study a rather singular oscillator often appearing in semiconductor optical cavities, i.e., a self-pulsing (SP) limit-cycle, and its synchronization to an external periodic signal. This self-sustained oscillator can be understood as the result of a dynamical interplay between two or more nonlinear mechanisms that can modify the optical mode effective refractive index<sup>12–16</sup>. The SP limit-cycle usually takes energy from the continuous laser used to excite a specific optical mode and, therefore, is prone to be injection-locked to a signal actuating on an optical modulator placed in the incoming optical path. This work analyses both experimentally and numerically the specific case of thermo-optic/free-carrier-dispersion SP, which emerges routinely in silicon-based optical cavities at sufficiently high laser powers<sup>14,16</sup>. We perform our study in optomechanical crystal cavities (OMC), since the SP oscillator can be further employed to drive a mechanical mode into the lasing regime by exploiting the temporal modulation of the radiation pressure force<sup>17</sup>. The first part of the manuscript studies the synchronization of the SP to the radio-frequency (RF) tone when the mechanical degrees of freedom are damped using the fiber optical probe. Special attention is paid to the interaction between higher harmonics both of the SP, which is highly anharmonic by nature, and of the perturbation, which deviates from harmonicity as the perturbation amplitude increases. We find that synchronization is achieved in a very broad bandwidth (60% of its natural frequency), surpassing other approaches for external locking<sup>18–21</sup>. In the last part of the work we study the SP mechanism and its injection-locking mechanism when the OMC is mechanically liberated. In the latter context, we find that mechanical modes whose frequency lies far away from that of the SP can be driven to the lasing regime just by tuning the frequency of the SP with the RF modulation and then switching the latter off. We discuss the implications of these findings for acoustic signal generators based on NOEMS in a monolithic silicon platform, which enable an enhanced control over the spatial shape, amplitude and frequency of the generated signals.

## Results and discussion

**General properties of the sample and experimental considerations.** In our study, we consider a silicon OMC nanobeam cavity described in the “Methods” section<sup>22</sup>. We employ a two-wavelength continuous-wave pump and probe optical setup to characterize the non-linear dynamics of the optically-driven silicon nanobeam (see Fig. 1a). The pump laser (labelled L1) excites the fundamental optical mode of the OMC at  $\lambda_{1,o} = 1531$  nm and activates the nonlinear dynamics within the optical cavity, while the probe (labelled L2) is resonant with the first-order optical mode at  $\lambda_{2,o} = 1559$  nm and is used to monitor the optical cavity dynamics. A low-power optical transmission spectrum of the OMC is shown in Fig. 1b, evidencing the two modes with optical Q factors of  $3.1 \times 10^4$  and  $0.8 \times 10^4$  respectively. Both

lasers are linearly polarized with fiber polarizer controllers (FPC) to match the polarization of the OMC cavity modes. Optical signals decoupled from the OMC are spectrally filtered by means of tunable Fabry-Perot filters (WF) with a pass-band of about 1 nm and detected in the photodiodes (PD) either in transmission or reflection. Given that the wavelength filters are aligned with L2, the detected signal solely comprises the cavity dynamics and not the direct modulation of L1 (the out-band suppression is >40 dB).

The electric signals of the PDs are analysed with an oscilloscope (OSC), a spectrum analyzer (SA) and a vector network analyzer (VNA). The VNA is also used to drive a Mach-Zehnder modulator (EOM), having a half-wave voltage  $V_\pi = 6.7$  V, which modulates in amplitude the output of L1. The offset voltage ( $V_{DC}$ ) is set at the quadrature point  $V_{DC} = 0.5 V_\pi$  to minimize higher harmonics in the perturbation (details in Methods). The voltage applied to the EOM thus reads:

$$V(t) = V_{\max} \sin(2\pi f_{\text{mod}} t) + V_{DC} \quad (1)$$

The SP oscillator embedded within the OMC cavity can be described by two coupled first order differential equations governing the temporal evolution of the free-carrier-population ( $N$ ) and the effective temperature ( $\Delta T$ ) within the cavity region of the OMC<sup>16</sup>:

$$\dot{N} = -\Gamma_{FC} N + \alpha_{SPA} n_o (N_o - N) \quad (2)$$

$$\dot{\Delta T} = -\Gamma_T \Delta T + \alpha_{FC} n_o N$$

where  $\alpha_{SPA}$  is the rate of free-carrier density increase per photon and unit of density of available intragap states and  $\alpha_{FC}$  is the rate temperature increase per photon and unit free-carrier density. The first differential equation considers Single-Photon Absorption (SPA) through the  $N_o$  intragap states per unit volume and a surface recombination rate given by  $\Gamma_{FC}$ . The second equation considers Free-Carrier-Absorption (FCA) and a heat dissipation mechanism characterized by a rate  $\Gamma_T$ . Although it plays a role in the number of generated carriers in our OMCs, we have not considered two-photon absorption because our evidences of the FCA loss increase per intracavity photon points towards a dominating SPA mechanism in the OMCs under study (details in Methods). Both equations are coupled through the number of intracavity photons ( $n_o$ ), which includes both the cavity resonance filtering effect and the external perturbation induced by the EOM as described in Eq. (1) and in the “Methods” section. Under these considerations,  $n_o$  reads:

$$n_o(t) = n_{o,m}(N) \left( 1 - \sin\left(\pi \frac{V_{\max} \sin(2\pi f_{\text{mod}} t)}{V_\pi}\right) \right) \frac{\Delta\lambda_1(N)^2}{4(\lambda_{L1} - \lambda_1(N, \Delta T))^2 + \Delta\lambda_1(N)^2} \quad (3)$$

where we neglect optical temporal delays due to the relatively low optical quality factors. The first mode resonant wavelength reads  $\lambda_1(N, T) \approx \lambda_{1,o} - \frac{\partial\lambda_1}{\partial N} N + \frac{\partial\lambda_1}{\partial T} \Delta T$  and includes first order thermo-optic and free-carrier-dispersion effects. The number of intracavity photons when the voltage applied to the EOM is  $V = V_{DC} = 0.5 V_\pi$  and the L1 wavelength is in perfect resonance ( $\lambda_{L1} = \lambda_1$ ) is denoted by  $n_{o,m}$  and is set to be in the order of  $10^4$  by adjusting the laser power. The modulation percentage is experimentally quantified in the oscilloscope when the fibre is not coupled to the OMC and is given by  $P_{\text{mod}} = \pm 100 \sin\left(\frac{\pi V_{\max}}{V_\pi}\right)$ . Both  $n_{o,m}$  and the linewidth of the resonance  $\Delta\lambda_1$  account for the intrinsic optical loss increase associated mainly to FCA and hence proportional to  $N$ . Indeed, FCA losses have been experimentally evaluated as an increase of  $\Delta\lambda_1$  when  $n_o$  increases (details in Methods) and inserted in the model. Even under the assumptions made, the complexity of Eq. (3) hinders the analytical study of the solutions of Eq. (2). Therefore, we have restricted our study of

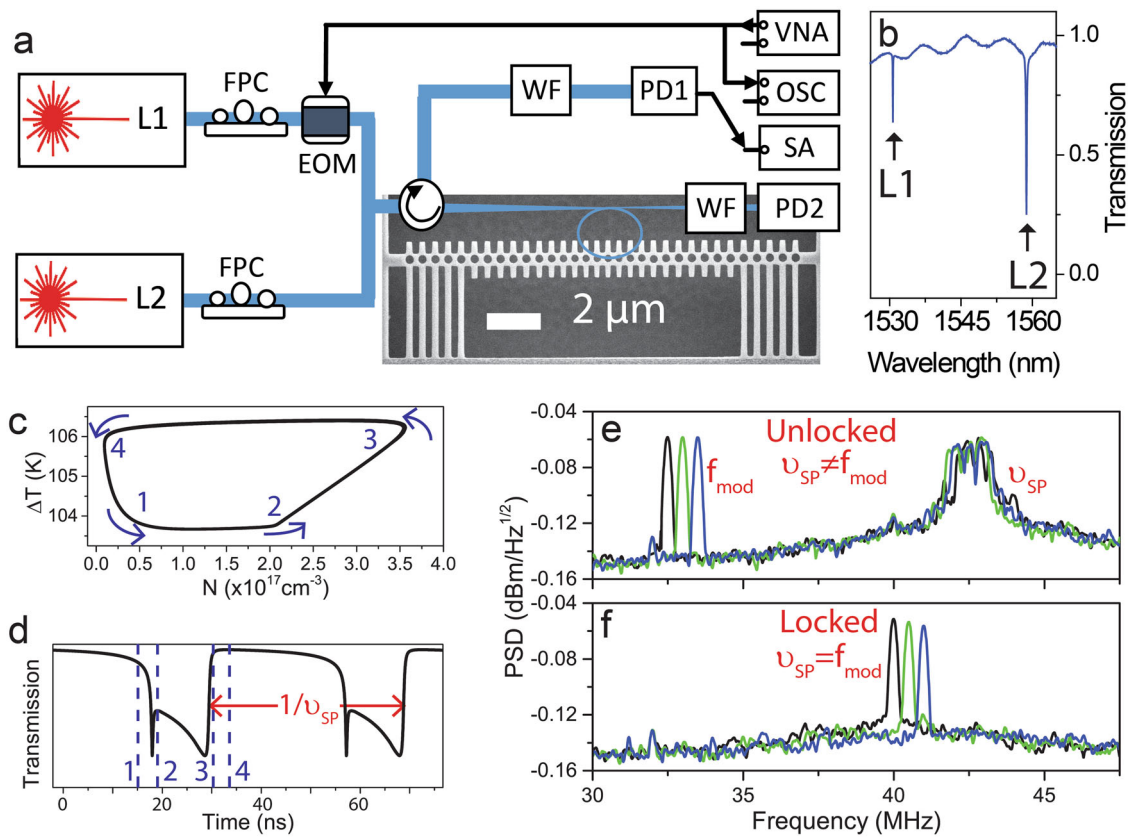


**Fig. 1 Experimental setup and principle of operation.** **a** The main optical signals are derived from two external-cavity diode lasers (L1 and L2) and sent into a tapered microloop optical fiber to evanescently couple light into the silicon optomechanical crystal cavity (OMC). The optical signal decoupled from the OMC is collected by the same fiber and measured either in transmission or in reflection using an in-fiber circulator. The signals in both arms are band-pass filtered by 1 nm bandwidth wavelength filters (WF), impinging on two fast photodetectors (PDs). The electrical signals are sent to a spectrum analyzer (SA), a vector network analyzer (VNA) or an oscilloscope (OSC) for characterization. EOM stands for electro-optic modulator and FPC for fiber polarization controller. **b** Optical transmission spectrum, exhibiting two optical modes at  $\lambda_{1,o} = 1531$  nm and  $\lambda_{2,o} = 1559$  nm. Lasers L1 and L2 address the fundamental and first order modes respectively, L1 acting as the pump and L2 as the probe. **c** Self-pulsing (SP) limit-cycle represented in the phase space defined by the effective temperature increase of the cavity region ( $\Delta T$ ) and the free carrier concentration ( $N$ ) **d** Time trace of the transmitted optical signal when SP is active. The positions highlighted by numbers 1–4 are associated to the different corners of the SP limit-cycle of panel **c**. **e** and **f** Power spectral density (PSD) spectra when the system is in a SP state and the modulation is on ( $P_{mod} = \pm 6.1\%$ ) at different modulation frequencies. In panel **e** the SP limit-cycle is not locked to the external modulation ( $f_{mod} = 33$  MHz and  $v_{SP} = 43$  MHz), while it is locked in panel **f** ( $f_{mod} = v_{SP} = 41$  MHz).

Eqs. (2) and (3)) to numerical simulations (see Supplementary Notes 1 and 2), which unavoidably misses unstable solutions. In the absence of external modulation ( $\dot{V} = 0$ ) the stable solution is the SP limit-cycle<sup>16</sup> that is active for a wide range of the L1 laser parameters, namely its power and  $\lambda_{L1}$ . Its phase-space diagram and the resulting temporal transmission trace are illustrated in Fig. 1c, d, respectively. The natural frequency of such closed trajectory ( $v_{SP}$ ) can be tailored in a wide range varying the L1 laser parameters<sup>16</sup>, which is a feature that anticipates the ductility of the SP oscillator in view of its response to a periodic external perturbation. It is worth to note that the SP is only perturbed by the external modulation between points 1 and 3, i.e., when light is coupled into the cavity. Typical examples of the experimental RF spectra when the SP limit-cycle is phase-unlocked or phase-locked to external RF tones are depicted in Fig. 1e, f, respectively.

**Self-pulsing oscillator and injection locking mechanism.** In the following we provide further insight of the dynamics of the SP oscillator and the synchronization mechanism in a framework common to other standard nonlinear oscillators in presence of harmonic perturbations. An analysis of the time required to go over the different numeric points highlighted in Fig. 1c and d reveals that the SP limit-cycle parametrized in terms of  $N$  and  $\Delta T$

is not drawn at constant pace. We therefore define a generalized phase of the SP oscillator along the limit-cycle that increases monotonously with time as  $\phi(t) = 2\pi v_{SP} t$ . Within this framework it would eventually be possible to derive an Adler equation<sup>3</sup> in a rotating system that would describe the temporal evolution of the phase difference between the SP oscillator as defined above and the phase of an external force ( $2\pi f_{mod} t$ ) in the vicinity of a resonance condition  $f_{mod} \approx \frac{m}{n} v_{SP}$ , where  $m$  and  $n$  are integers without a common divisor. It would read:

$$\dot{\psi} = -\Delta + \varepsilon q(\psi) \tag{4}$$

where  $\psi = \phi - 2\pi f_{mod} t$  and  $\Delta = 2\pi(f_{mod} - v_{SP,mod-off})$  is the frequency detuning between the external signal and the SP limit-cycle in the absence of modulation ( $v_{SP} = v_{SP,mod-off}$  in that case). The second term on the right hand side of Eq. (4) accounts for the perturbation related to the modulation of L1,  $\varepsilon$  being a parameter quantifying its strength that is related to  $P_{mod}$  and  $q(\psi)$  a  $2\pi$ -periodic function containing the quasi-resonant terms<sup>1</sup>. Synchronization to the external perturbation implies a stable fixed point on Eq. (4), i.e.,  $\dot{\psi} = 0$  so that  $\phi$  experiences a constant rotation at a frequency equal to  $f_{mod}$ . The range of  $\Delta$  along which the latter condition is held is known as the Arnold tongue.



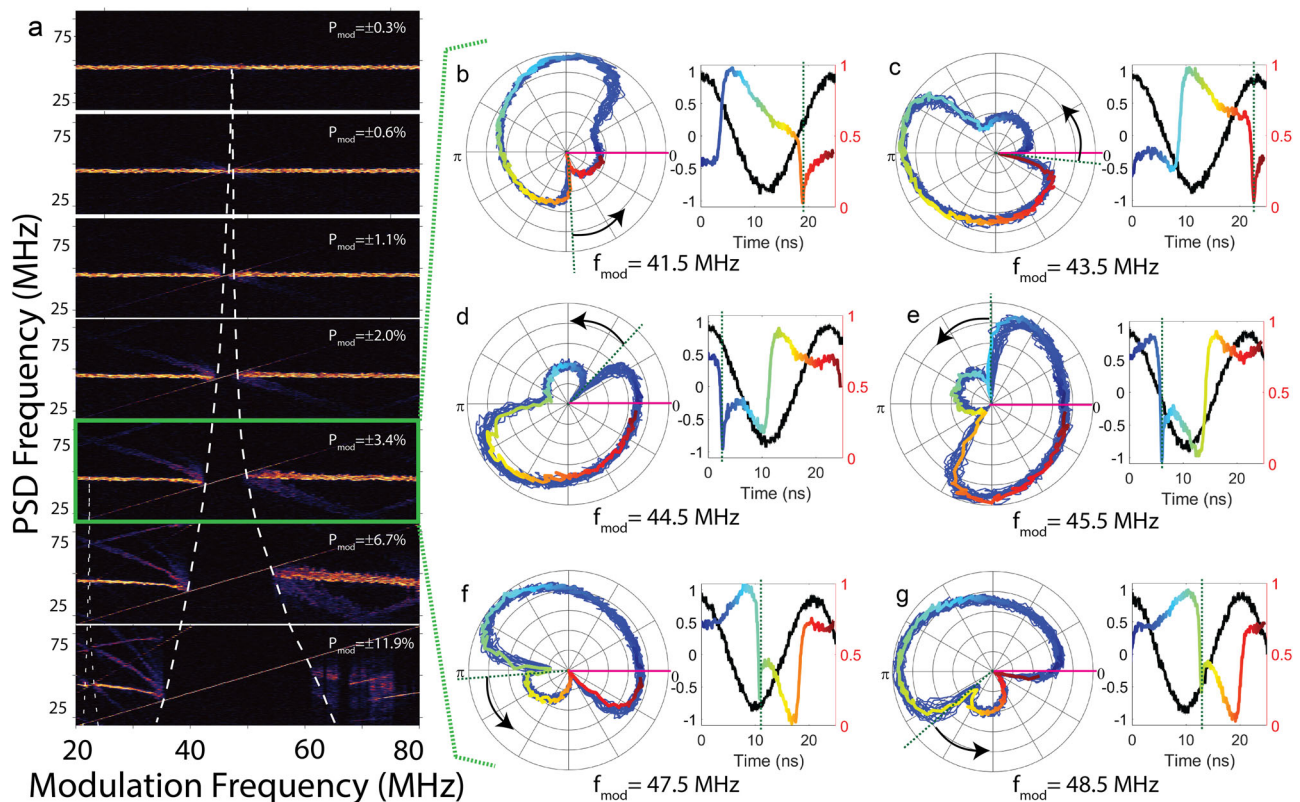


**Fig. 2 Arnold tongues.** **a** Colormaps of the power spectral density (PSD) of transmitted light for modulation amplitudes from  $P_{\text{mod}} = \pm 0.3\%$  to  $P_{\text{mod}} = \pm 11.9\%$ . The dashed white lines are guides to the eye to illustrate the growth of the Arnold tongues. **b–g** (Left subpanels) Time traces of the transmission signal in a polar representation, where the distance to the center is the transmission amplitude value and the angle is the phase difference with respect to the maximum of the modulation signal. The total temporal register used for this representation is  $0.5 \mu\text{s}$ . (Right subpanels) Time traces of the normalized modulation signal (black) and transmission signal (coloured scale). The modulation amplitude is  $P_{\text{mod}} = \pm 3.4\%$  and each panel corresponds to a different modulation frequency within the Arnold tongue, covering most of its spectral width. Dashed green lines indicate the position of the faster transmission minimum, i.e., slightly before point 2 of Fig. 1c and d. A common-coloured scale has been used for the transmission curves in each couple of subpanels.

In most of the self-sustained systems studied in literature prone to display synchronization, such as the well-known Van der Pol or Duffing oscillators, synchronization to an external reference can occur via two main mechanisms: phase-locking or suppression of natural dynamics. Phase-locking is the most common one and derives from a saddle-node bifurcation in which the natural limit-cycle would transform into two fixed points, one stable and one unstable, and generally occurs for small frequency detunings and perturbation strengths. The dynamics of the original system is only altered in terms of a frequency-entrainment with the external perturbation<sup>1,2</sup>. On the other hand, synchronization by suppression of natural dynamics generally occurs for large frequency detunings and perturbation strengths, where the stable fixed point originates from the shrinking of the natural limit-cycle onto an unstable fixed point<sup>2</sup>. Consequently, synchronization by suppression implies that the natural dynamics of the oscillator is greatly altered not only in phase but also in amplitude so that the dynamics within the Arnold Tongue is a stable fixed point mostly determined by the perturbation. Although, to the best of our knowledge, there is not a general mathematical formalism describing those two synchronization mechanisms, there are several features common to specific nonlinear self-sustained systems. Indeed, it is possible to recognise experimentally and numerically the synchronization mechanism by analysing the evolution of the frequency spectrum and by means of stroboscopic sections<sup>2</sup>, the latter being sets of points of the phase trajectory taken with a sample rate equal to  $f_{\text{mod}}$ . We have applied that analysis to our system to identify the synchronization mechanism.

**Experimental characterization of the injection locking mechanism.** The path towards entering the Arnold Tongue can be done either by gradually reducing  $\Delta$  and/or by increasing  $\epsilon$ . If synchronization is achieved through a phase-locking mechanism, the frequency peak associated to natural oscillations is frequency-pulled towards that of the perturbation along the path until it frequency-locks, while in the case of suppression it does not move but becomes weaker until it finally vanishes leaving just the perturbation peak<sup>2</sup>. Following this procedure, we have analysed the spectral dependence of the power spectral density (PSD) when the SP is active at  $\nu_{\text{SP}} \sim 43$  MHz and  $f_{\text{mod}}$  is shifted between 20 and 80 MHz (scanning of  $\Delta$ ) for different values of  $P_{\text{mod}}$  (scanning of  $\epsilon$ ). This set of measurements is shown in the different subpanels of Fig. 2a and reveals an increasing size of the Arnold tongue with  $P_{\text{mod}}$  (main dashed white line) as well as its asymmetric growth, i.e., a larger lock range at  $f_{\text{mod}} > \nu_{\text{SP}}$ . An important observation is that the peak associated with natural SP dynamics appearing at  $\nu_{\text{SP}}$  does not significantly degrade and can move by several tens of percent its initial value to coincide with  $f_{\text{mod}}$  even for the largest  $P_{\text{mod}}$  value displayed in Fig. 2a. This is, as mentioned above, a signature of phase-locking regardless of the large values of  $\Delta$  and  $\epsilon$ . Numerical simulations of Eq. (2) qualitatively reproduce the experimental spectral behaviour with stroboscopic analysis of the simulated temporal traces giving further indications of the phase-locking nature of the synchronization (details in Methods). Simulations of the nonlinear dynamics obtained by numerically solving Eq. (2) allow to

qualitatively reproduce the experimental spectral behaviour including the asymmetry of the Arnold Tongue with  $P_{\text{mod}}$  (see the “Methods” section). The latter feature originates from high-order synchronization peaks<sup>20</sup>, which are especially relevant here due to the specific anharmonic nature of the SP dynamics. Across the Arnold tongue, the SP limit-cycle adapts its relative phase with respect to the modulation so that the region between points 1 and 3 of the cycle (see Fig. 1c, d) are aligned with a high modulation value if the locking frequency is low and vice versa (Supplementary Fig. 4). The size of the SP limit-cycle in the  $N$ - $\Delta T$  phase space changes significantly its size with respect to the natural case, being larger at low locking frequencies and smaller at the other side of the Arnold tongue (Supplementary Fig. 3), thus explaining the giant locking range of the SP oscillator. This is possible thanks to the large time interval with negligible  $N$  and  $n$  and slowly cooling  $\Delta T$ , which leaves room for a modification of the time interval between two pulses. This behaviour contrasts with other types of oscillators, where the perturbation is present along the whole cycle and the phase trajectory only slightly deviates from the original one. Moreover, by analysing the simulated temporal data of  $N$  and  $\Delta T$  with the stroboscopic technique at  $f_{\text{mod}}$  (Supplementary Figs. 1 and 2), we observe that the phase trajectory before entering the synchronization region does not change meaningfully and that the fixed point is born on its surface, which is a further indication of phase-locking. The phase noise of the SP limit-cycle greatly improves within the Arnold tongue, reaching  $-100$  dBc Hz<sup>-1</sup> at 10 kHz (details in Methods) at  $P_{\text{mod}} = \pm 11.9\%$ , which is similar to the values reported by us in an injection-locked OMC oscillator<sup>19</sup>.

The secondary Arnold tongue that appears experimentally at  $f_{\text{mod}} \sim v_{\text{SP}}/2$ , which is also highlighted in Fig. 2a, is of much smaller bandwidth than the main one. This is an expected feature since, as stated above, the modulation signal is configured to suppress higher harmonics so that the resonant conditions embedded within the Adler equation (Eq. (4)) are in principle only met when  $f_{\text{mod}} \approx mv_{\text{SP}}$ . The fact that this secondary Arnold tongue appears at all is related with the small deviation of the modulation signal from harmonicity and/or with the fact that the perturbation is filtered by the dynamics of the cavity resonance. Although the experimental configuration ensures filtering out the optical signal coming from L1, there is still a small contribution at  $f_{\text{mod}}$  in phase with the EOM associated to a resonant modulation of the temperature of the cavity regardless of being inside or outside the Arnold tongue, which prevents a precise analysis of the SP phase using the VNA. Therefore, we have used the oscilloscope to analyse the evolution of the relative phase between the EOM and the SP signal along the Arnold tongue, avoiding the quasi-sync regions placed at its extremes<sup>18</sup>. These results are displayed in Fig. 2b–g for different values of  $f_{\text{mod}}$ , where the right subpanels represent the time traces of the modulation and transmission signals (black and coloured respectively). Both traces are taken simultaneously using the first one as a trigger signal in the oscilloscope. The left subpanels display the transmission signal in a polar representation suitable to avoid self-intersections and to superimpose all the full cycles recorded in the transmission temporal trace. The radius is associated to the limit-cycle optical transmission trace and the angle to the relative phase of the harmonic modulation signal with respect to its maximum, i.e., we express the reference signal as  $\cos(2\pi f_{\text{mod}}t)$ , where  $2\pi f_{\text{mod}}t$  is the polar angle of the plot. This is equivalent to the stroboscopic technique described above but using the whole temporal trace instead of sampling only one phase point. To better illustrate this, the transmission curves have been plotted in both subpanels with a common colour scale linked to each phase point. Taking the position of the fast transmission minimum as reference (green

dashed line), which happens between points 1 and 2 of the limit-cycle displayed in Fig. 1d, there is an overall phase shift along the Arnold tongue greatly exceeding  $\pi$ . The latter magnitude has been measured for different values of  $P_{\text{mod}}$  and there is an overall  $\pi$  phase shift for  $P_{\text{mod}} < 2.4\%$  while, for  $P_{\text{mod}} > 2.4\%$  it increases to more than  $3\pi$  for the largest  $P_{\text{mod}}$  value (details in Methods). This is at odds with what is stated and measured in the literature for standard phase-locking based systems, where if the synchronization region is “crossed” along the line of constant  $\epsilon$  the phase shift varies by  $\pi$ <sup>1–3,18–21,23</sup>. Moreover, when analysing this feature in the numerical simulations, the overall phase shift is also  $\pi$  even for large  $P_{\text{mod}}$  values. This experimental result is likely related again with the anharmonic nature of both the SP and the perturbation at high modulation values, which, as we show later, leads to very efficient injection-locking even between higher harmonics. This pinpoints the fact that locking between the fundamental harmonic of both SP and the RF tone may not dominate throughout the Arnold tongue, thus leading to distinct cycling of  $\psi$  across the tongue.

When expanding the modulation frequency range, we have observed that SP can also be locked to the external reference by means of higher harmonics of the SP signal, i.e., when  $f_{\text{mod}} \approx mv_{\text{SP}}$ . This is a consequence of the anharmonicity of the SP limit-cycle, which largely overcomes that of other standard nonlinear oscillators such as the Van der Pol or the Duffing<sup>24</sup>. Figure 3 reports a set of data recorded both with the SA (panel a) and with the VNA (black curve of panel b) using a modulation frequency range between 10 and 500 MHz for  $P_{\text{mod}} = \pm 1.1\%$ , which shows synchronization to the external signal for  $m$  values up to 11 (see Supplementary Note 3, where time traces up to  $m = 5$  are showed in Supplementary Fig. 7). Indeed, the VNA magnitude spectrum shows a plateau as long as the  $m^{\text{th}}$  harmonic of the SP is synchronized with the external signal at  $f_{\text{mod}}$ , the spectral widths of which define the Arnold tongues. A comparison with the PSD spectrum of the SP without modulation measured with the SA (red curve of Fig. 3b) confirms that  $S_{21}$  plateaus appear around SP harmonics and that their intensity decays with a similar trend although the noise of the PSD measurement masks the presence of SP harmonics larger than  $m = 4$ . Unexpectedly, the spectral width of the Arnold tongues measured in  $S_{21}$  increases with  $m$  up to  $m = 3$  and  $v_{\text{SP}}$  is frequency pulled by a larger extent for  $m = 2, 3$  than for  $m = 1$ . This feature gives a hint to explain the previous observation displayed in Fig. 2b–e of overall phase-shifts exceeding  $\pi$  along the Arnold tongue as discussed above, given that at large modulation amplitudes the perturbation becomes anharmonic and the SP could lock to the external signal by means of higher harmonics, i.e.,  $m^{\text{th}}$  harmonic of the external signal with  $m^{\text{th}}$  harmonic of the SP. It is noteworthy that the minima observed in  $S_{21}$  above 200 MHz are likely associated to destructive interference between a contribution of direct modulation, which also decays with frequency, and the locked-SP signals. Also, a small drift of the SP natural frequency is observed in Fig. 3a since the set of data required hours of acquisition time.

**Exploitation of injection locking to reach elusive dynamical attractors.** To illustrate a possible application of the wide frequency-locking range of the SP dynamics, in the following we mechanically liberate the OMC by removing its physical contact with the fiber, hence adding to Eq. (2) two equations associated to a mechanical harmonic oscillator driven by radiation pressure forces. The full system is governed by the set of four first-order nonlinear differential equations coupled through  $n_o$  described extensively in our previous works<sup>16,17</sup>. If a mechanical mode with

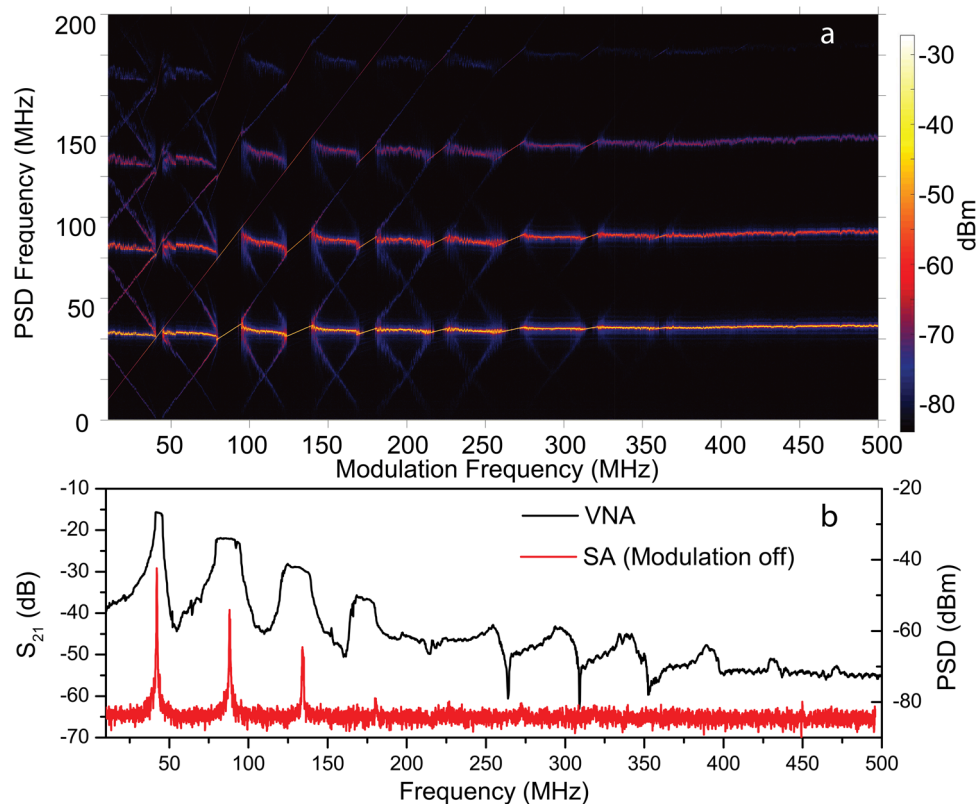


**Fig. 3** Injection locking to higher self-pulsing harmonics. **a** Colour contour plot of the power spectral density (PSD) spectra as a function of the modulation frequency covering a range between  $f_{\text{mod}} = 10$  MHz and 500 MHz to for a modulation amplitude of  $P_{\text{mod}} = \pm 3.4\%$ . The PSD power is quantified in dBm in the colour scale. **b** Coherent frequency response of the reflected optical signal ( $S_{21}$ ) measured in the vector network analyzer (VNA) as a function of the modulation/detection frequency (black curve, left axis) and PSD spectra measured in the spectrum analyzer (SA) when the modulation is off (red curve, right axis).

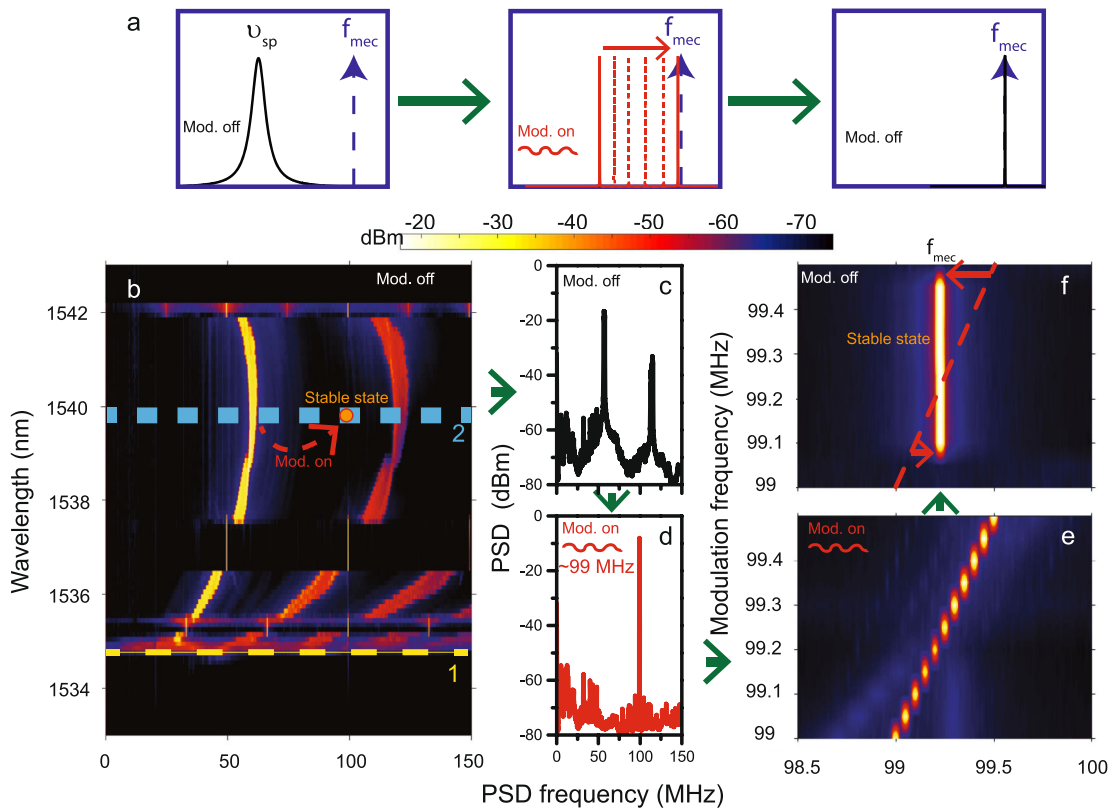
eigenfrequency  $f_{\text{mec}}$  is partially resonant with one of the harmonics of the SP, it can be driven into mechanical lasing provided that the OM coupling rate is sufficiently large. Moreover, by means of the OM coupling strength, the mechanical motion frequency-locks the SP so that  $\nu_{\text{SP}}$  is forced to be a simple fraction of the mechanical eigenfrequency, which is a feature that resembles what occurs when the external modulation is on and the SP locks to it. Indeed, once the mechanical mode is in a high amplitude state, it can be also understood as an anharmonic modulator of  $n_o$  through the OM coupling mechanism. The largest amplitude mechanical lasing oscillation can be obtained by using the main harmonic so that  $\nu_{\text{SP}} = f_{\text{mec}}$ . Here, it is interesting to remark that, as a consequence of the robustness of  $f_{\text{mec}}$  in comparison with the SP natural frequency, OM systems driven to a mechanical lasing state display injection-locking bandwidths about three orders of magnitude narrower<sup>19,25,26</sup> than that of the SP limit-cycle reported above for similar modulation amplitudes.

Figure 4a shows a schematic of the performed experiment, in which the system is initialized in a SP limit-cycle with  $\nu_{\text{SP}}$  far from a mechanical mode with eigenfrequency  $f_{\text{mec}}$  (left panel). The modulation is then switched on so that SP is locked to it and  $f_{\text{mod}}$  is increased until being close to  $f_{\text{mec}}$  (central panel). The modulation is finally switched off and the system can be left in a mechanical lasing state at  $f_{\text{mec}}$  (right panel). Figure 4b shows a 2D colour plot of the PSD spectra in the absence of external modulation as a function of the wavelength of L1 ( $\lambda_{L1}$ ). Below the dashed yellow line, several thermally activated mechanical modes can be optically transduced, among which the in-plane flexural mode with three antinodes ( $f_{\text{mec}} = 99.3$  MHz) shows the largest OM coupling rate, which is dominated by the moving interface

contribution<sup>27</sup>. The dashed yellow line also indicates the wavelength threshold above which the SP limit-cycle is activated. As described above,  $\nu_{\text{SP}}$  corresponds to the frequency of the first harmonic of the signal and varies with  $\lambda_{L1}$ , reaching a maximum at  $\nu_{\text{SP}} = 54$  MHz (Fig. 4b), which is far from  $f_{\text{mec}}$ . Under these conditions, mechanical lasing can be achieved only using the third or the second harmonic of the optical force, i.e., for  $\nu_{\text{SP}} = f_{\text{mec}}/3$  and  $\nu_{\text{SP}} = f_{\text{mec}}/2$ , respectively. The mechanical lasing dynamics appears in Fig. 4b as frequency plateaus where the specific harmonic of the SP is locked to the coherent oscillation of the mechanical mode. In a similar fashion to what is shown in Fig. 2a, by switching on the external modulator with  $P_{\text{mod}}$  values on the order of  $\pm 13\%$  it is possible to synchronize the SP on a wide spectral range reaching more than 60% its natural value (Fig. 4d, e). Therefore, it is possible for  $\nu_{\text{SP}}$  to reach  $f_{\text{mec}}$  and activate the coherent oscillation of the mechanical mode of interest, the signatures of which appear in the PSD spectrum in the form of weak sidebands around the main RF peak at  $f_{\text{mec}}$  and at  $2^*f_{\text{mod}}f_{\text{mec}}$ . This particular region has been studied by us in a previous work<sup>19</sup>.

Figure 4f illustrates the final dynamical state of the system after switching off the modulation using a 2D colour plot of the PSD spectra as a function of the modulation frequency when it was on (red dashed line). Thus, each spectrum of Fig. 4f can be directly compared to its counterpart when the modulation was on in Fig. 4e. Our results indicate that there is a range of  $f_{\text{mod}}$  above and below  $f_{\text{mec}}$  where, after the modulation is switched off, the system ends up in a stable mechanical lasing state in which the mechanical mode is oscillating at large amplitudes at and the SP is frequency-locked so that  $\nu_{\text{SP}} = f_{\text{mec}}$ . This means that there is a stable attractor of the system that was not possible to achieve





**Fig. 4 Exploitation of injection locking to reach a mechanical lasing state.** **a** Scheme of the experiment. **b** Colour contour plot of the power spectral density (PSD) spectra as a function of the laser (L1) wavelength ( $\lambda_{L1}$ ) when the modulation is off. The horizontal dashed line denoted by 1 (yellow) indicates the threshold for the self-pulsing activation, while that denoted by 2 (cyan) refers to the configuration associated to rest of the panels of this figure. The PSD power is quantified in dBm with the same colour scale as in Fig. 3a. **c, d** PSD spectrum when the modulation is off (**b**) and on at about 99 MHz and  $P_{\text{mod}} = \pm 13\%$  (**c**). Colour contour plot of the PSD spectra as a function of the modulation frequency when the modulation is on (**e**) and after it has been switched off (**f**). The dashed line in (**f**) indicates the frequency of the state when the modulation was on. The PSD power of (**b**), (**e**) and (**f**) is quantified in dBm in the colour scale.

just by modifying the laser parameters. The spectral range of  $f_{\text{mod}} - f_{\text{mec}}$  leading to stable mechanical lasing presents a clear asymmetry towards positive values that is highlighted in Fig. 4f with a longer red arrow on the right side than on the left. On the left side the system is attracted towards opposite directions by the lasing and the SP attraction basins so that the final state depends on the overall strength. On the other hand, on the right side both basins attract the system towards lower frequencies, thus intersecting the lasing attraction basin in its way. This reasoning could lead to expect an absence of a cut off on the high modulation frequency side, but the decay rate at which the system intersects the lasing state basin increases with the modulation frequency, so that after some point the system just cuts across without giving enough time for the mechanical coherent oscillation dynamics to build up and lock the SP there. In that case the system dynamics continues its way towards the natural SP state. We have also observed these features in our numerical simulations (see Supplementary Figures 5 and 6). It must be noted that the liberated OMC can also be locked to a fraction of  $f_{\text{mod}}$  by synchronizing higher harmonics of the SP signal to the external reference as in Fig. 3, which was demonstrated by us<sup>19</sup> and by other groups in silicon nitride optomechanical microdisks<sup>26</sup>.

## Conclusions

We have studied the synchronization to an external signal of a thermal/free-carriers SP limit-cycle occurring in a silicon optomechanical crystal cavity. This is a system with unique features when compared to other self-sustained nonlinear systems subject to external periodic perturbations, the most obvious one being

that it does not own a robust natural oscillation frequency explicitly appearing in the equations. We have identified that the synchronization mechanism is of the phase-locking type, instead of suppression of the natural dynamics. Synchronization of the SP at subharmonics of the external signal has revealed as a very effective mechanism, in some cases even more than at the main harmonic, thus suggesting the possible use of this system for frequency division purposes<sup>28,29</sup>, which often demand low-power consumption and wide-band operation<sup>30</sup>.

For modulation amplitudes exceeding 10% we have measured Arnold tongues with a spectral width greatly exceeding half of the natural frequency of the oscillator. This feature opens the possibility of exploring usually inaccessible dynamical attractors of the system by tailoring the SP frequency externally. Indeed, we have experimentally pulled the SP frequency more than 60% its natural value in a mechanically-free optomechanical crystal cavity so that it fell in the vicinity of the mechanical lasing attraction basin of a mechanical mode of interest. Under these circumstances the system can remain in a mechanical lasing stable state after the modulation has been switched off. This is a very appealing feature for nano-electro-opto-mechanical-system (NEOMS) coherent mechanical signal generators, since a specific mechanical mode of interest (because of its frequency and/or spatial shape) could be chosen to remain in a lasing state. On the other hand, we have observed that sub- and super-harmonic synchronization also appears in the liberated OMC, which also paves the way of developing NEOMS frequency converters for applications in integrated microwave photonics.

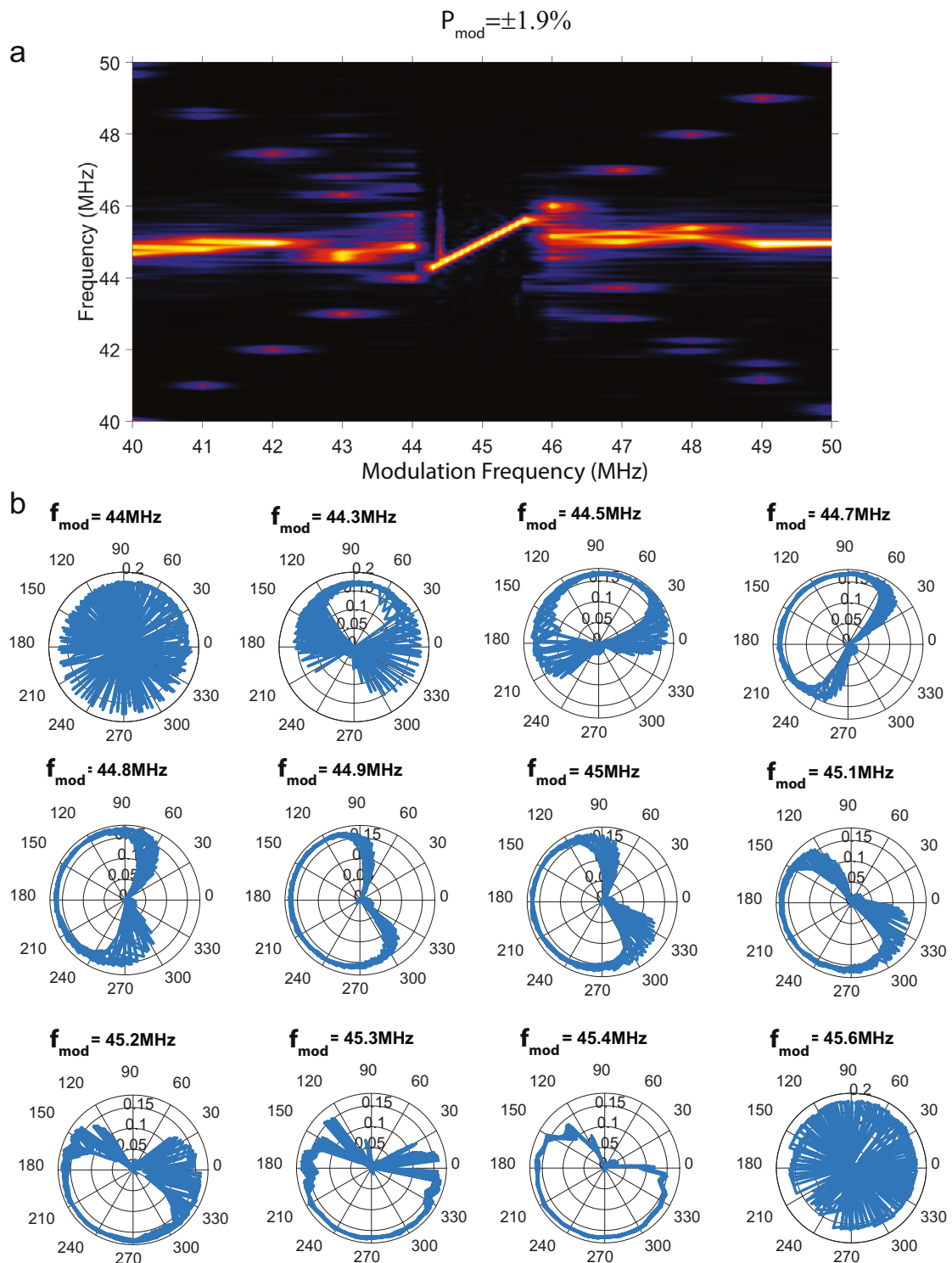


**Fig. 5 Arnold tongue for a modulation amplitudes of  $P_{\text{mod}} = \pm 1.9\%$ .** **a** Colormap of the power spectral density (PSD). **b** Time traces of the transmission signal in a polar representation, where the distance to the center is the transmission value and the angle is the phase difference with respect to the maximum of the modulation signal. Each panel corresponds to a different modulation frequency, covering the spectral width of the Arnold tongue.

## Methods

**Design and fabrication of the optomechanical crystal cavity.** The geometry of the Optomechanical Crystal Cavity (OMC) is based on a unit cell consisting of a parallelogram with a cylindrical hole in the center and two symmetric stubs on the sides as shown in the scanning electron microscope (SEM) image of Fig. 1a. The cavity region in the center of the nanobeam consists of 12 cells with the pitch ( $a$ ), the radius of the holes ( $r$ ) and the length of the stubs ( $d$ ) decreasing quadratically towards the center of the beam. Periodic mirrors are placed on both sides of the

central region. The nominal geometrical values of the cells of the mirror are  $a = 500$  nm,  $r = 150$  nm and  $d = 250$  nm. The ratio of the geometrical parameters of the central cell with respect to that of the mirror cells is 0.85. The five outer cells at each side of the crystals are clamped to the silicon frame, so that the in-plane flexural modes are decoupled from the frame and confined to the central region of the OMCs. The fabrication process of the OMCs uses standard silicon-on-insulator nanofabrication processes described in detail elsewhere<sup>22</sup>. After patterning, the nanobeam is released by removing the oxide layer beneath the beam.



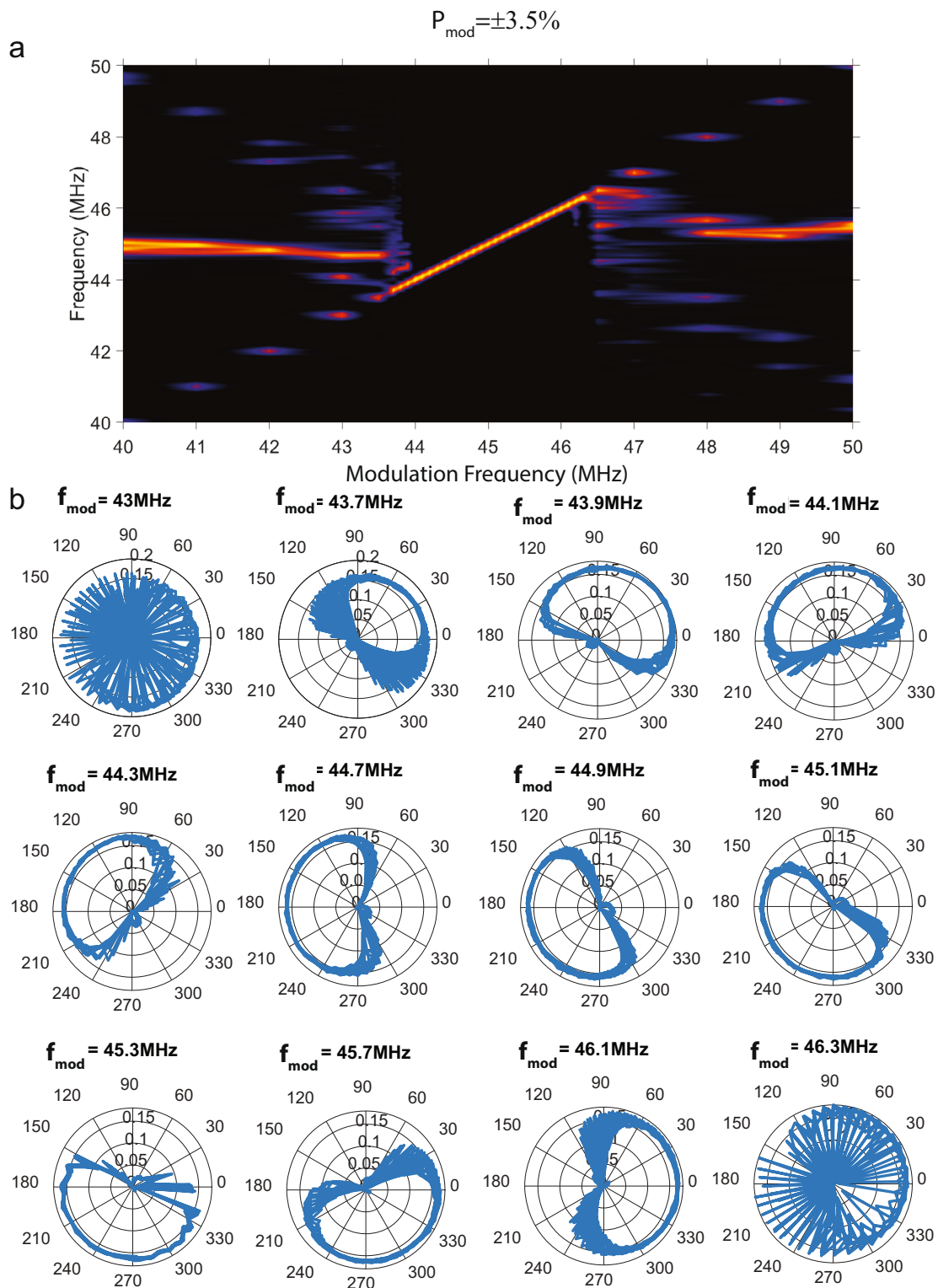


**Fig. 6 Arnold tongue for a modulation amplitudes of  $P_{\text{mod}} = \pm 3.5\%$ .** **a** Colormap of the power spectral density (PSD). **b** Time traces of the transmission signal in a polar representation, where the distance to the center is the transmission value and the angle is the phase difference with respect to the maximum of the modulation signal. Each panel corresponds to a different modulation frequency, covering the spectral width of the Arnold tongue.

**Experimental measurements of the overall phase shift along the Arnold tongue.** We have measured the overall phase shift between the SP limit-cycle and the reference modulation signal along the Arnold tongue for several modulation values. As explained in the main text, these measurements were registered with an oscilloscope by using the reference signal as trigger signal. In the present case, the used oscilloscope owns a bandwidth of 500 MHz instead of 4 GHz, which was the case of Fig. 2 of the main text. By comparing Figs. 5a with 6a we can observe the

enlargement of the Arnold tongue by increasing  $P_{\text{mod}}$  reported in Fig. 2. On Figs. 5b and 6b we observe that the characteristic shape depicted by the optical transmission when it is synchronized with external reference indeed rotates counter clockwise. At  $P_{\text{mod}} = \pm 1.9\%$  (Fig. 5b) the overall rotation is around  $\pi$ , but at  $P_{\text{mod}} = \pm 3.5\%$  (Fig. 6b) this magnitude clearly exceeds  $\pi$ . We have done the same study for various  $P_{\text{mod}}$  values between  $\pm 1\%$  and  $\pm 13\%$  and summarized the results in Fig. 7. We observe an overall  $\pi$  phase shift for  $P_{\text{mod}} < 2.4\%$  while, for

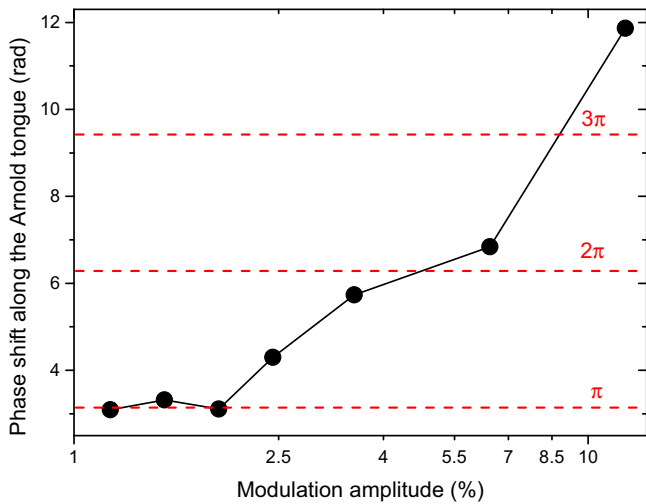


**Fig. 7 Accumulated phase difference across the width of the Arnold tongue versus the modulation percentage.** The plotted values account for the overall phase shift of the transmission curve with respect to the reference signal when going across the injection-locking frequency range. Dashed red lines highlight integer multiples of  $\pi$ .

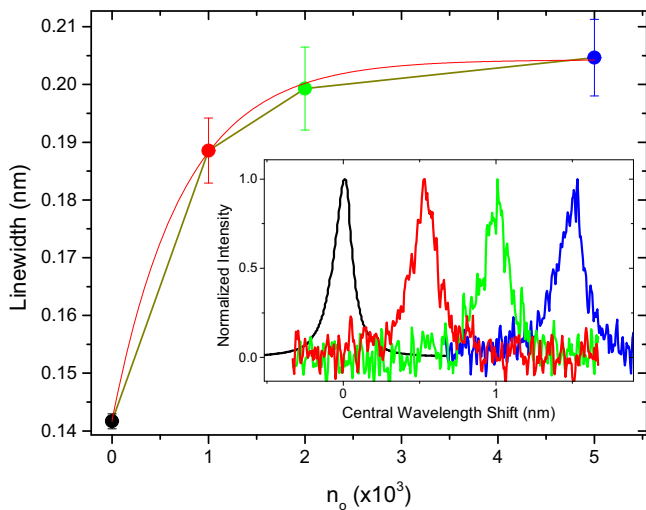


**Fig. 8 Free carrier related optical losses.** Evolution of the optical linewidth of the first cavity mode with respect to the number of intracavity photons populating the second cavity mode. The red curve is a fit to the experimental data using Eq. (5). The inset shows the first optical resonance and its spectral shift when the number of intracavity photons is increased. The Lorentzian fit of those peaks was used to extract the linewidths values of the main panel. The colour code of the curves in the inset is linked to the number of intracavity photons of the points of the main panel. The vertical error bars in the main panel are associated to the quality of the lorentzian fit of the curves in the inset.

$P_{mod} > 2.4\%$ , it monotonously grows up with  $P_{mod}$  to more than  $3\pi$  for the largest  $P_{mod}$  value.

**Dependence of the optical losses with the number of intracavity photons.** The overall optical losses of the cavity depend on the number of intracavity photons, which, as explained in the text, create free-carriers that increase free-carrier absorption (FCA). Optical losses are directly related with  $N$ , which adds complexity to Eq. (2), since this impacts both to  $n_{o,m}$  and to the total linewidth of the resonance  $\Delta\lambda_1$ . Hence, along the limit-cycle both magnitudes change their value in a periodic way with frequency  $\nu_{SP}$  when the SP limit-cycle is active.

We have experimentally verified the impact of FCA by using a pump and probe technique similar to that employed elsewhere<sup>19</sup>. L2 is used now to

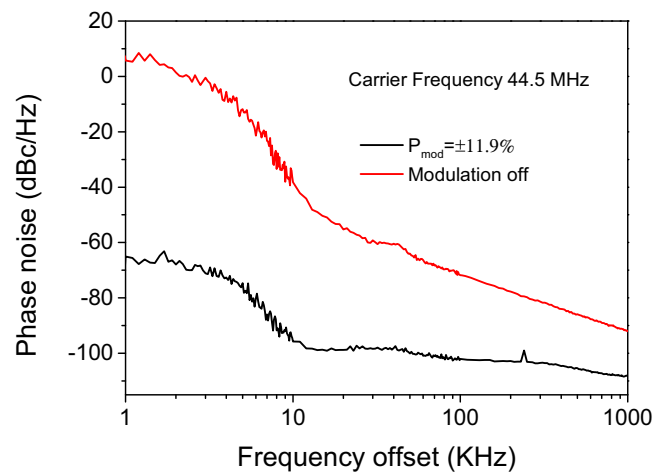


**Fig. 9 Phase noise of the injection-locked oscillator.** Phase noise measurements of the free-running self-pulsing (SP) oscillator (red curve) and of the injection-locked SP with a radio-frequency external tone at 44.5 MHz with modulation amplitudes  $P_{mod} = \pm 11.9\%$  (black curve).

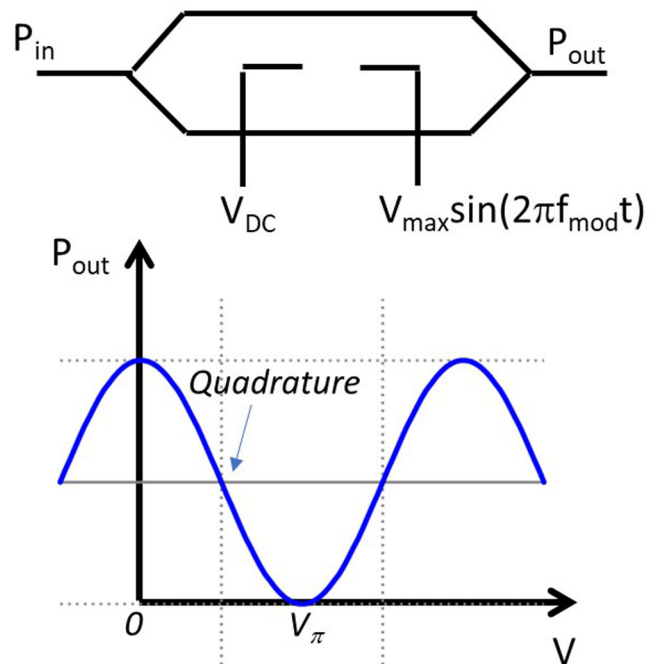


**Fig. 10 Layout of the Mach Zehnder modulator.** The DC voltage ( $V_{DC}$ ) sets the quadrature point of the modulator at  $V_{\pi}/2$  so that, if the maximum voltage of the RF modulation signal ( $V_{max}$ ) is small, the output light power ( $P_{out}$ ) responds linearly to the RF modulation signal. Notice that the overall voltage applied to the modulator is given by  $V_{DC} + V_{max}\sin(2\pi f_{mod}t)$ .

introduce a large number of photons in the second mode of the cavity, while L1 is scanned with very low power to measure the optical linewidth of the first cavity mode without introducing any dispersive effect associated to temperature or free-carriers. To filter out the contribution of L2 to the detected signal we have used a lock-in technique at low frequency (10 KHz) to modulate and detect the signal associated to L1. To increase  $n_o$  we gradually enter the second cavity resonance as the L2 wavelength is increased. As a consequence, there are both dispersive and dissipative effects that impact the first mode as well, the former leading to a red-shift of the resonance due to the dominance of thermo-optic effects (inset to Fig. 8) and the latter to the widening of  $\Delta\lambda_1$  (main panel of Fig. 8). We have fitted the observed trend with a saturating function (red curve of main panel of Fig. 8) reading:

$$\Delta\lambda_1 = AN = A \frac{N_o \alpha_{SPA} n_o / \Gamma_{FC}}{1 + \alpha_{SPA} n_o / \Gamma_{FC}}, \tag{5}$$

which is consistent with a SPA model in which we drain the intragap states from carriers as stated in Eq. (2) of the main text,  $A$  being a proportionality constant relating  $N$  and  $\Delta\lambda_1$ .

Moreover, the number of intracavity photons in perfect resonance reads:

$$n_{o,m} = 2P_{in}\lambda_{1,0}\kappa_e/\kappa^2hc, \quad (6)$$

where  $P_{in}$  is the input laser power, and  $\kappa$  and  $\kappa_e$  are the overall and extrinsic loss rates, respectively. By introducing the identity  $\kappa = \lambda_1^2\Delta\lambda_1/2\pi c$  in Eqs. (5) and (6) we get the relation between  $n_{o,m}$  and  $N$ :

$$n_{o,m} = 8\pi^2P_{in}\lambda_{1,0}\kappa_e c \left/ \left( \lambda_1^2 A \frac{N\alpha_{SPA}n_o}{1 + \frac{I_{FC}}{I_{FC}}} \right)^2 \right. h \quad (7)$$

**Phase noise of the injection-locked self-pulsing.** The phase noise spectrum of the injection-locked SP reaches values around  $-100$  dBc Hz $^{-1}$  at 10 kHz (black curve of Fig. 9) along the phase-locking bandwidth, which is on the same range of what we observed elsewhere<sup>19</sup> in an injection-locked OMC oscillator. However, the injection-locked OMC oscillator displayed much better phase-noise figures below 10 kHz. The phase noise of the free running SP oscillator (red curve of Fig. 9) is several orders of magnitude larger.

**Mach-Zehnder modulator output power.** A scheme of the Mach Zehnder modulator that we use in our experimental setup is displayed in Fig. 10, where, in one of the arms, we apply a DC voltage ( $V_{DC}$ ) to operate in a quadrature point and a RF harmonic signal.

The output power can thus be written as:

$$P_{out} = \frac{P_{in}}{2} \left( 1 + \cos \left( \pi \frac{(V_{max} \sin(2\pi f_{mod}t) + V_{DC})}{V_{\pi}} \right) \right) \quad (8)$$

If  $V_{DC} = 0.5 V_{\pi}$ , then the expression reduces to:

$$P_{out} = \frac{P_{in}}{2} \left( 1 - \sin \left( \pi \frac{V_{max} \sin(2\pi f_{mod}t)}{V_{\pi}} \right) \right) \quad (9)$$

## Data availability

All the data that support the plots and the other findings of this study are available from the corresponding author upon reasonable request.

## Code availability

All the computational codes that were used to generate the data presented in this study are available from the corresponding author upon reasonable request.

Received: 13 April 2022; Accepted: 8 December 2022;

Published online: 17 December 2022

## References

- Pikovsky, A., Kurths, J., Rosenblum, M. & Kurths, J. *Synchronization: a universal concept in nonlinear sciences* (Cambridge University Press, 2003).
- Balanov, A., Janson, N., Postnov, D. & Sosnovtseva, O. *Synchronization: from simple to complex* (Springer Science & Business Media, 2008).
- Adler, R. A study of locking phenomena in oscillators. *Proc. IEEE* **61**, 1380–1385 (1973).
- Kurokawa, K. Injection locking of microwave solid-state oscillators. *Proc. IEEE* **61**, 1386–1410 (1973).
- Paciorek, L. J. Injection locking of oscillators. *Proc. IEEE* **53**, 1723–1727 (1965).
- Stover, H. L. Theoretical explanation for the output spectra of unlocked driven oscillators. *Proc. IEEE* **54**, 310–311 (1966).
- Armand, M. On the output spectrum of unlocked driven oscillators. *Proc. IEEE* **57**, 798–799 (1969).
- Hossain, M. & Carusone, A. C. CMOS oscillators for clock distribution and injection-locked deskew. *IEEE J. Solid-State Circuits* **44**, 2138–2153 (2009).
- Shekhar, S. et al. Strong injection locking in low-Q LC oscillators: modeling and application in a forwarded-clock I/O receiver. *IEEE Trans. Circuits Syst. I: Regul. Pap.* **56**, 1818–1829 (2009).
- Rategh, H. R. & Lee, T. H. Superharmonic injection-locked frequency dividers. *IEEE J. Solid-State Circuits* **34**, 813–821 (1999).

- Imani, A. & Hashemi, H. Distributed injection-locked frequency dividers. *IEEE J. Solid-State Circuits* **52**, 2083–2093 (2017).
- Baker, C. et al. Optical instability and self-pulsing in silicon nitride whispering gallery resonators. *Opt. Express* **20**, 29076–29089 (2012).
- Soltani, M., Yegnanarayanan, S., Li, Q., Eftekhari, A. A. & Adibi, A. Self-sustained gigahertz electronic oscillations in ultrahigh-Q photonic microresonators. *Phys. Rev. A (Coll. Park)* **85**, 53819 (2012).
- Johnson, T. J., Borselli, M. & Painter, O. Self-induced optical modulation of the transmission through a high-Q silicon microdisk resonator. *Opt. Express* **14**, 817–831 (2006).
- Fomin, A. E., Gorodetsky, M. L., Grudinin, I. S. & Ilchenko, V. S. Nonstationary nonlinear effects in optical microspheres. *JOSA B* **22**, 459–465 (2005).
- Navarro-Urrios, D. et al. A self-stabilized coherent phonon source driven by optical forces. *Sci. Rep.* **5** (2015).
- Navarro-Urrios, D. et al. Self-sustained coherent phonon generation in optomechanical cavities. *J. Opt.* **18** (2016).
- Razavi, B. A study of injection locking and pulling in oscillators. *IEEE J. Solid-State Circuits* **39**, 1415–1424 (2004).
- Arregui, G. et al. Injection locking in an optomechanical coherent phonon source. *Nanophotonics* **10**, 1319–1327 (2021).
- Amitai, E., Lörch, N., Nunnenkamp, A., Walter, S. & Bruder, C. Synchronization of an optomechanical system to an external drive. *Phys. Rev. A (Coll. Park)* **95**, 53858 (2017).
- Hossein-Zadeh, M. & Vahala, K. J. Observation of injection locking in an optomechanical rf oscillator. *Appl. Phys. Lett.* **93**, 191115 (2008).
- Gomis-Bresco, J. et al. A one-dimensional optomechanical crystal with a complete phononic band gap. *Nat. Commun.* **5**, 4452 (2014).
- Pitanti, A. et al. Strong opto-electro-mechanical coupling in a silicon photonic crystal cavity. *Opt. Express* **23**, 3196–3208 (2015).
- Andronov, A. A. & Vitt, S. E. K. *Theory of Oscillations* (Pergamon, 1966).
- Bekker, C., Kalra, R., Baker, C. & Bowen, W. P. Injection locking of an electro-optomechanical device. *Optica* **4**, 1196–1204 (2017).
- Rodrigues, C. C. et al. Optomechanical synchronization across multi-octave frequency spans. *Nat. Commun.* **12**, 5625 (2021).
- Johnson, S. G. et al. Perturbation theory for Maxwell's equations with shifting material boundaries. *Phys. Rev. E* **65**, 66611 (2002).
- Mercadé, L. et al. Testing optomechanical microwave oscillators for SATCOM application. *J. Lightwave Technol.* **40**, 4539–4547 (2022).
- Mercadé, L., Morant, M., Griol, A., Llorente, R. & Martínez, A. Photonic frequency conversion of OFDM microwave signals in a wavelength-scale optomechanical cavity. *Laser Photon Rev.* **15**, 2100175 (2021).
- Amann, A., Mortell, M. P., O'Reilly, E. P., Quinlan, M. & Rachinskii, D. Mechanism of synchronization in frequency dividers. *IEEE Trans. Circuits Syst. I: Regul. Pap.* **56**, 190–199 (2009).

## Acknowledgements

This work was supported by the MICINN project ALLEGRO (PID2021-124618NB-C21 and PID2021-124618NB-C22).

## Author contributions

D.N.-U. performed the experiments. D.N.-U. and N.E.C. developed the model and analysed the data. G.A., M.F.C., A.P., J.J.F., L.M. and A.M. participated in the experiments at different stages. A.G. and A.M. fabricated the samples. All authors contributed to the interpretation of the results and writing of the manuscript.

## Competing interests

The authors declare no competing interests.

## Additional information

**Supplementary information** The online version contains supplementary material available at <https://doi.org/10.1038/s42005-022-01113-9>.

**Correspondence** and requests for materials should be addressed to Daniel Navarro-Urrios.

**Peer review information** *Communications Physics* thanks Aranya B. Bhattacharjee and the other, anonymous, reviewer(s) for their contribution to the peer review of this work. Peer reviewer reports are available.

**Reprints and permission information** is available at <http://www.nature.com/reprints>

**Publisher's note** Springer Nature remains neutral with regard to jurisdictional claims in published maps and institutional affiliations.



**Open Access** This article is licensed under a Creative Commons Attribution 4.0 International License, which permits use, sharing, adaptation, distribution and reproduction in any medium or format, as long as you give appropriate credit to the original author(s) and the source, provide a link to the Creative Commons license, and indicate if changes were made. The images or other third party material in this article are included in the article's Creative Commons license, unless indicated otherwise in a credit line to the material. If material is not included in the article's Creative Commons license and your intended use is not permitted by statutory regulation or exceeds the permitted use, you will need to obtain permission directly from the copyright holder. To view a copy of this license, visit <http://creativecommons.org/licenses/by/4.0/>.

© The Author(s) 2022